Chemical Science

ROYAL SOCIETY OF CHEMISTRY

EDGE ARTICLE

View Article Online
View Journal | View Issue

Check for updates

Cite this: *Chem. Sci.*, 2021, **12**, 6378

All publication charges for this article have been paid for by the Royal Society of Chemistry

Received 27th February 2021
Accepted 31st March 2021

DOI: 10.1039/d1sc01163d

rsc.li/chemical-science

Non-stackable molecules assemble into porous crystals displaying concerted cavity-changing motions†

Taewon Kang, ‡[a] Hongsik Kim, ‡[a] Sungeun Jeoung, ‡[b] Dohyun Moon, *[c] Hoi Ri Moon *[b] and Dongwhan Lee *[a]

With small molecules, it is not easy to create large void spaces. Flat aromatics stack tightly, while flexible chains fold to fill the cavities. As an intuitive design to make open channels inside molecularly constructed solids, we employed propeller-shaped bicyclic triazoles to prepare a series of aromatic-rich three-dimensional (3D) building blocks. This modular approach has no previous example, but is readily applicable to build linear, bent, and branched arrays of non-stackable architectural motifs from existing flat aromatics by single-pot reactions. A letter H-shaped molecule thus prepared self-assembles into porous crystals, the highly unusual stepwise gas sorption behaviour of which prompted in-depth studies. A combination of single-crystal and powder X-ray diffraction analysis revealed multiple polymorphs, and sterically allowed pathways for their reversible interconversions that open and close the pores in response to external stimuli.

Introduction

To construct stress-resistant structures, rigid and shape-persistent building blocks are needed. Otherwise, the assembly would easily collapse. The same principle holds for making non-collapsible open channels by stacking up individual molecules.[1–4] With appropriate design, such supramolecular constructs can change the size, shape, and dimension of the pores without compromising their overall architectural integrity, so that small guests can be captured and released by using external stimuli.[5–11] From a design perspective, what kind of molecular shape is ideal for such adaptivity? In this paper, we provide a practical answer to this question.

Planar aromatic molecules are rigid, but they tend to engage in tight π–π contacts.[12–14] As such, they are the least amenable choice of building blocks to make porous materials. How could one spatially organize flat slabs so that they cannot stack well and always leave voids in between? A macroscopic object that

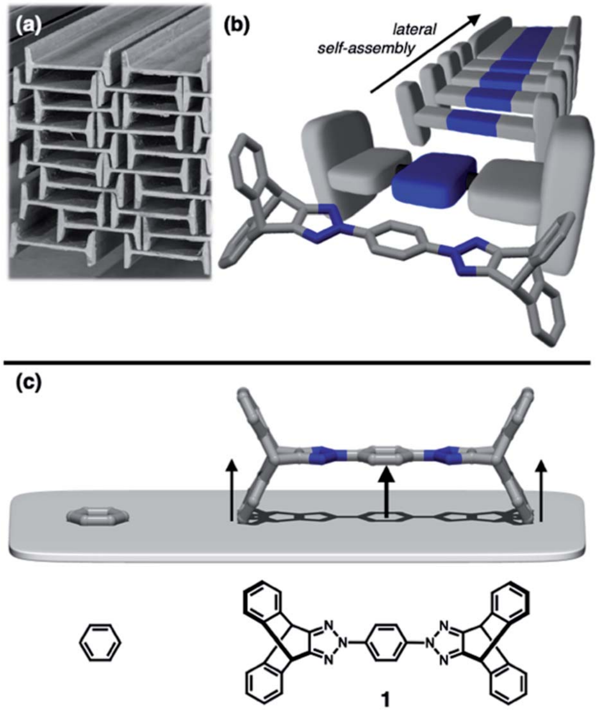

Fig. 1 (a) Stacks of steel H-beams leaving non-collapsible open channels, which inspired (b) molecular-level construction of H-beams by lateral self-assembly. (c) Chemical structure of the building block **1**, in which two iptycene units are appended to "lift up" the benzene core. In (b), the blue-coloured horizontal slab of the H-shaped 3D model corresponds to the electron-deficient triazole–phenyl–triazole triad within **1**, the capped-stick representation of which is overlaid for clarity.

---

[a] Department of Chemistry, Seoul National University, 1 Gwanak-ro, Gwanak-gu, Seoul 08826, Korea. E-mail: dongwhan@snu.ac.kr

[b] Ulsan National Institute of Science and Technology (UNIST), 50 UNIST-gil, Eonyang-eup, Ulji-gun, Ulsan 44919, Korea

[c] Pohang Accelerator Laboratory, 80 Jigokro-127-beongil, Nam-gu, Pohang 37673, Korea

† Electronic supplementary information (ESI) available: Experimental procedures and additional data (^{1}H and ^{13}C NMR spectra, FT-IR spectra, HR-MS) of the newly synthesized compounds. CCDC 1980363–1980368, 2048700, and 2048701. For ESI and crystallographic data in CIF or other electronic format see DOI: 10.1039/d1sc01163d

‡ T. Kang, H. Kim, and S. Jeoung contributed equally to this work.

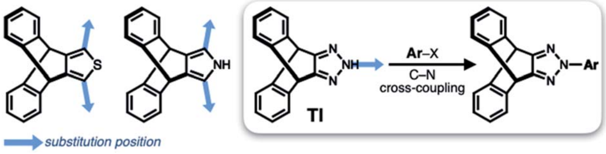

Scheme 1 Covalent modification of heteroaromatic-fused iptycenes.

satisfies this design requirement is the H-beam used for steel framed buildings (Fig. 1a). Due to the orthogonal relationship between the planes, stacks of letter H-shaped objects should always make edge-to-face contacts, thereby leaving behind a linearly extended empty space, regardless of how they are packed. The size and shape of the resulting channels would change if the H-beams are allowed to slide relative to each other.

Background and design principles

Translated into molecular language, however, it is impossible to elongate an H-beam to an infinite length by covalent bonds. A synthetically more viable approach would be creating a molecule that resembles a thin slice of H-beam, and laterally connecting each other by non-covalent bonds (Fig. 1b). To turn this idea into reality, we have devised a modular synthetic route for "jacking up" the flat aromatic core by appending propeller-shaped molecular fragments at the periphery (Fig. 1c). This convergent synthesis requires efficient bond-making reactions between structural subcomponents with minimal interference from existing functional groups. For this purpose, we decided to exploit the C–N cross-coupling reactions[15] of triazoliptycene (**TI**)[16] and haloarenes (Scheme 1). Unlike other heteroaromatic variants[17–19] of the privileged iptycene motif,[5,20–23] the triazole-fused **TI** allows direct attachment of rigid bicyclic scaffolds onto existing aromatic core *via* single-bonds in the last stage in the synthesis. The highest level of synthetic modularity is achieved this way. A concise *point-to-point connection* between the vertices of five- and six-membered rings (Fig. 1 and Scheme 1) significantly expands the structural space of "iptycene-capped" aromatics, which are typically accessed by *edge-to-edge fusion* of two six-membered rings by condensation reactions.[20,23]

As the newest addition to the heteroaromatic-fused iptycene family, we recently reported the chemistry of **TI**.[16] By transition metal-catalyzed C–N cross-coupling reactions, a wide range of aryl groups can be installed at the N_2-position of **TI**.[15,16] As shown in Fig. 2a, one such molecule **PhTI** forms an antiparallel stacked "dimer" in the solid state to maximize donor–acceptor (D–A) type intermolecular π–π contacts between the electron-rich phenyl ring and the electron-deficient triazole ring.[16] A tightly packed array of dimeric $(\mathbf{PhTI})_2$ leaves no void space in the crystal lattice. We postulated that blocking the open end of the *N*-phenyl group of **PhTI** by installing additional **TI** units should effectively suppress the formation of a tightly stacked dimer, thereby opening up void space in the crystal lattice.

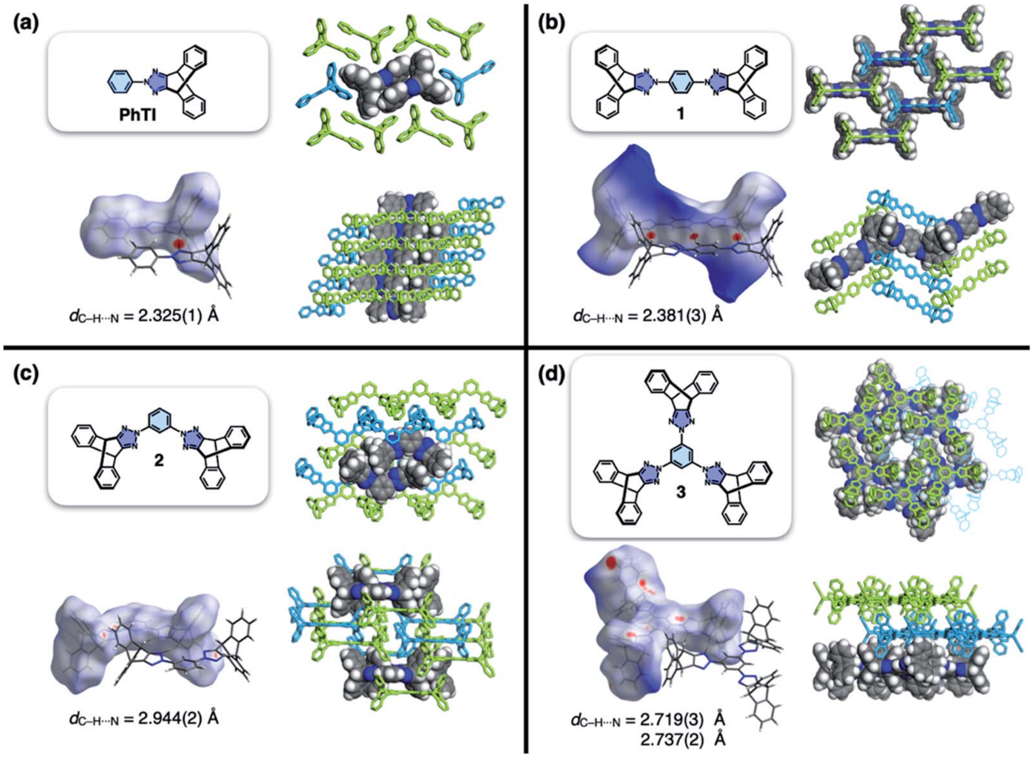

Fig. 2 Molecular structures, Hirshfeld surfaces[24] mapped with d_{norm} values, and single-crystal packing diagrams of (a) **PhTI**, (b) **1** (**1A** phase), (c) **2**, and (d) **3**, constructed with crystallographically determined atomic coordinates. Disordered solvent molecules are omitted for clarity. For each structure, the hydrogen bond length ($d_{C-H\cdots N}$) denotes the interatomic distance between hydrogen and nitrogen atoms.

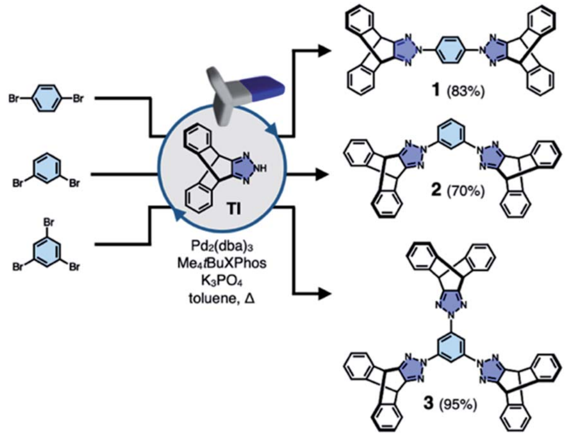

Scheme 2 Modular construction by one-pot C–N cross-coupling reactions.

Results and discussion

Non-stackable 3D aromatics: modular synthesis and solid-state assembly

To test the validity of this intuitive steric model, **TI** was subjected to palladium-catalyzed C–N cross-coupling reactions with di- or tribromobenzene to produce **1–3** in high yields (up to 95%, Scheme 2).

Single-crystal X-ray diffraction (SC-XRD) studies revealed that **1** indeed affords a porous structure having open channels (Fig. 2b), whereas its regioisomer **2** assembles into a non-porous structure with isolated voids failing to define continuous channels (Fig. 2c). A close inspection of the crystal structure showed that the crescent-shaped **2** makes tight van der Waals (vdW) contacts between the concave and convex faces of neighboring molecules (Fig. 2c). This shape complementary vdW interaction is reinforced by the C–H⋯N hydrogen bonds ($d_{\mathrm{C-H\cdots N}}$ = 2.944(2) Å, Fig. 2c), which is also observed for **3** having three **TI** units surrounding the central benzene ring (Fig. 2d). The molecule crystallizes to form a hexagonal packing held by C–H⋯N hydrogen bonds ($d_{\mathrm{C-H\cdots N}}$ = 2.719(3), 2.737(2) Å, Fig. 2d) but without open channels.

Comparative structure analysis of **1–3** (Fig. 2) points toward the importance of the H-shaped molecular geometry. Unlike **2** or **3**, molecule **1** assembles into a porous structure since it cannot find shape-complementary pairs from any orientations. The intermolecular interaction thus extends in the lateral direction to maximize the number of C–H⋯N hydrogen bonds ($d_{\mathrm{C-H\cdots N}}$ = 2.381(3) Å, Fig. 2b). By design, close π–π contacts are not allowed for the resulting H-beam like assemblies (Fig. 1); they instead utilize weak C–H⋯π interactions to surround open channels (Fig. 2b).

Open channels displaying stepwise gas sorption behaviour

To investigate the functional relevance of the open channels found in crystalline **1**, sorption isotherms were obtained for N_2, H_2, and CO_2 gases (Fig. S1a–c†). Prior to measurements, solid samples were activated to remove solvent molecules. Interestingly, **1** showed guest-dependent gas sorption behaviour. Double-step adsorption isotherm and desorption hysteresis were observed for N_2 ($T = 77$ K, Fig. S1a†), although **1** does not seem to have specific binding sites for N_2. Deviation from type I isotherm[25] is one of the prominent characteristics of structural dynamics during the sorption process.[26–33] In stark contrast, only desorption hysteresis was observed for H_2 gas (Fig. S1b†); simple type I adsorption occurred for CO_2 gas (Fig. S1c†).

Our attempts to understand this intriguing gas sorption behaviour were initially met with insistent and uninterpretable experimental results. For example, powder X-ray diffraction (PXRD) analysis on the thermally activated **1** produced what appears to be a hopelessly complicated intensity pattern that could not be modeled with the initially obtained SC-XRD structure of **1** (Fig. S1d†). More problematic was the batch-to-batch irreproducibility of the PXRD data of **1**, which suggested the presence of multiple crystalline domains within the bulk material. Apparently, the relative proportions of these putative polymorphs vary from batch to batch, depending on how the microcrystallites of **1** were prepared before sorption measurements.

Metastable porosity of interconverting polymorphs

To identify the polymorph that is responsible for the double-step N_2 sorption (Fig. S1a†), we first needed to decipher the complicated PXRD pattern. An exhaustive empirical screening was thus carried out by changing the conditions for (i) precipitating microcrystallites of **1** from the solution, and (ii) removing entrapped solvent molecules from the harvested material. During this investigation, a total of four polymorphs

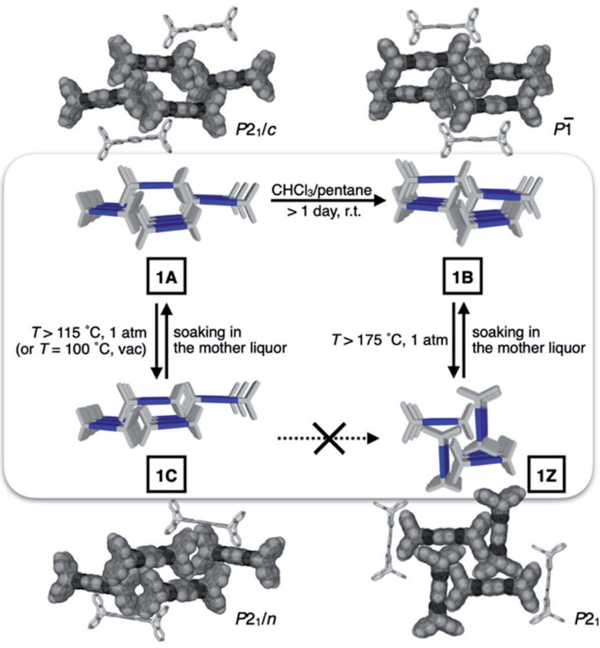

Fig. 3 Schematic representation of the structural interconversions between the four polymorphs. The capped-stick packing diagrams are constructed with crystallographically determined atomic coordinates, and overlaid with space-filling models to show intermolecular contacts and pores.

of **1** were identified, including the initially determined structure **1A** (Fig. 2b). All these polymorphs, **1A**, **1B**, **1C**, and **1Z**, were characterized by SC-XRD. The results are summarized in Fig. 3 and S2.†

We found that the addition of pentane into a chloroform solution sample immediately produced **1A,** whereas aging of the crystalline material in the mother liquor transformed it into **1B** (Fig. 3 and S3a†). Removal of entrapped solvents from **1A** and **1B** produced **1C** and **1Z**, respectively (Fig. 3, S3b and d†). These processes could be reversed, as evidenced by the PXRD analysis on the bulk sample prior to and after solvent back-filling (Fig. S3c and e†). The three polymorphs, **1A**, **1B**, and **1C**, have open channels as potential conduits for exogenous guests (Fig. 3). Even for the most tightly packed non-porous polymorph **1Z,** no close π–π contact could be established due to the geometrical mismatch between adjacent H-shaped building blocks (Fig. 3).

Structural dynamics captured during gas uptake and release

With the SC-XRD and PXRD data of the four polymorphs in hand, we proceeded to standardize the sample preparation and activation protocols to obtain reproducible gas sorption data. Specifically, samples of **1B** needed to be activated in a vacuum at $T = 100$ °C to achieve the prominent double-step adsorption isotherm and desorption hysteresis (Fig. 4a). Increasing the activation temperature induced **1B**-to-**1Z** conversion; the sample is fully transformed into non-porous **1Z** at $T = 175$ °C (Fig. 3 and S3d†). From the PXRD analysis of the bulk material used for gas sorption, we found that activated **1B** contains a small amount of **1C** phase (red asterisks; Fig. 4b and c). In addition, the entire structure was slightly perturbed, as reflected on the splitting of the (021) peak (green and blue asterisks; Fig. 4b and c), which is related to the plane bisecting the pores of **1B** phase (Fig. S4†). Except for this minor variation, other PXRD peaks of **1B** are fully maintained. Presumably, evacuation and heating in the activation process could shift the pores as the entrapped solvent molecules escape, but without significantly altering the cell parameters.

Changes in the PXRD patterns recorded under gas sorption conditions indicated the recovery of pure **1B** phase immediately after N_2 gas filled the vacuum (Fig. 4b and d). This phase transition is best interpreted as the pore-opening process that is responsible for the sharp increase in the V_{ads} *vs.* P/P_o curve at the very initial step ($P/P_o < 0.03$; Fig. 4a). At the second step ($P/P_o \approx 0.2$) where a sudden rise in gas uptake occurred again, however, the PXRD pattern does not show noticeable differences (Fig. 4d). In other words, this second structural transition involves only minor changes in the cell parameters yet a significant increase in the adsorption area. One possible explanation is an effective pore expansion by freezing out the bond-rotating

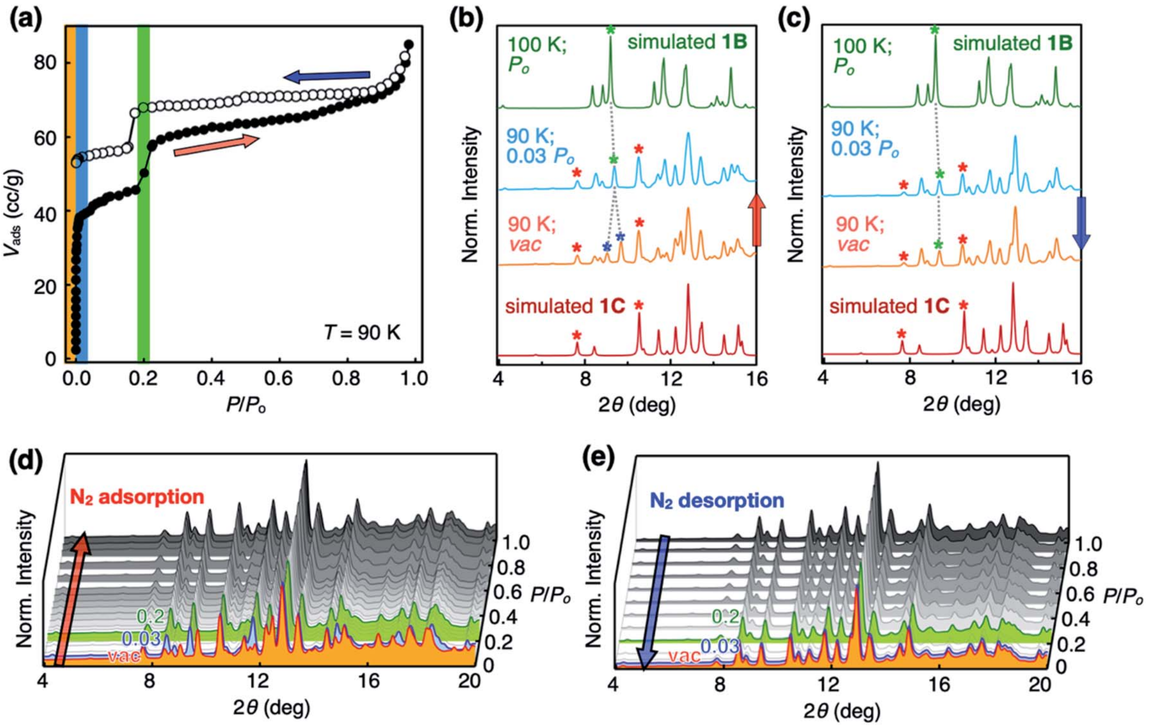

Fig. 4 N_2 sorption isotherms and *in situ* PXRD pattern changes recorded during the sorption process. (a) N_2 adsorption (filled circles; red arrow) and desorption (empty circles; blue arrow) isotherms of activated **1B** at $T = 90$ K showing double-step adsorption isotherm and desorption hysteresis. (b) Structural changes at the initial stage of N_2 uptake, as reflected on the two split (021) peaks (denoted by blue asterisks) merging into a single peak (denoted by a green asterisk), which indicates the recovery of the **1B** phase by pore-opening by N_2 molecules. Red asterisks denote small amount of **1C** phase formed during the activation process. (c) PXRD pattern at the final stage of N_2 desorption showing no noticeable changes of the (021) peak, which is consistent with the N_2 desorption hysteresis. PXRD pattern changes were recorded during the entire (d) adsorption, and (e) desorption processes.

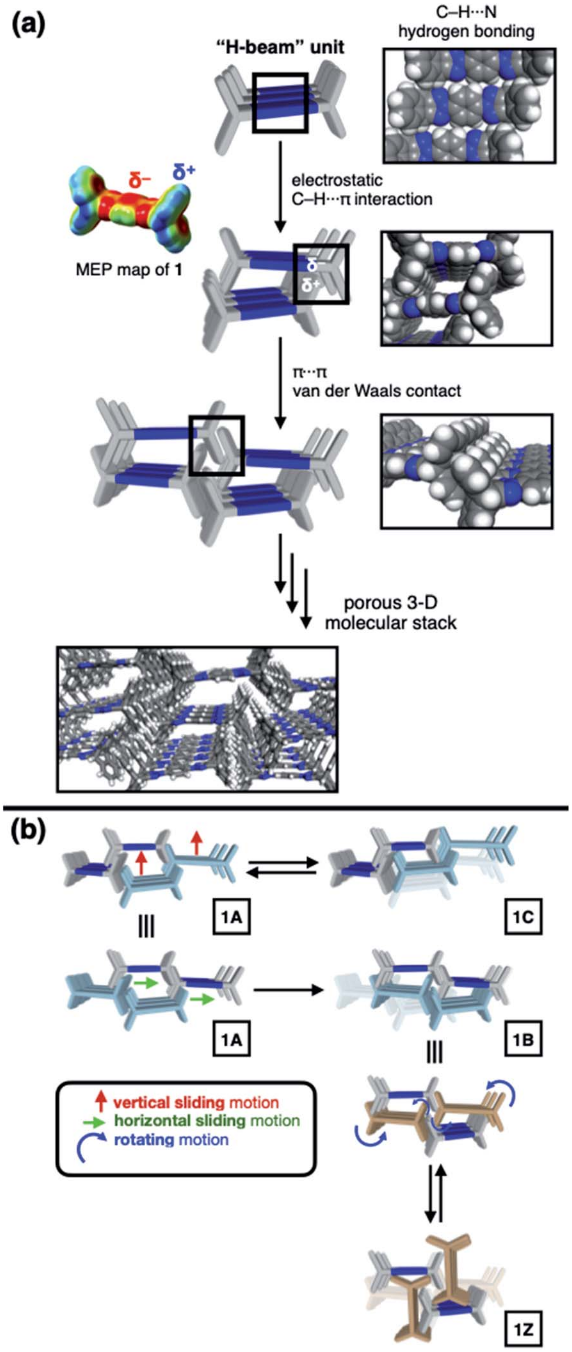

Fig. 5 (a) Schematic representation of lateral association of **1** to form H-beam units, and their organization into the 3-D lattice. At each stage of this conceptual reconstruction, space-filling models based on the X-ray structures of **1B** are shown next. The molecular electrostatic potential (MEP) map illustrates charge distribution that is responsible for intermolecular C–H···π interactions. (b) Synchronized sliding (either horizontal for **1A**-to-**1B**, or vertical for **1A**-to-**1C**) and rotating (for **1B**-to-**1Z**) motions of the H-beam units in the solid state to drive phase transitions.

motions[34–36] of the phenylene spacer group of **1**, which would have a negligible impact on the lattice constants.[35]

In the desorption process, no changes were observed in the PXRD pattern (Fig. 4c and e) at $P/P_o < 0.03$, indicating that gas sorption-induced structural transformation at low pressure is irreversible. This experimental observation is consistent with the hysteresis in the desorption process (Fig. 4a). Meanwhile, independently prepared crystals of **1C** displayed simple type I isotherm (Fig. S5†), thus ruling out its participation in the double-step sorption process.

Molecular origin of cavity-changing motions

To gain a detailed molecular-level understanding of the pore-changing motions observed in gas sorption, we revisited the solid-state intermolecular interactions captured by SC-XRD on the different phases of **1**. As summarized in Fig. 5a, all four phases share a common hierarchical assembly pattern involving three types of intermolecular forces: hydrogen bonding, electrostatic contact, and vdW interaction. Conceptually, the solid-state packing commences with lateral self-assembly of **1** by C–H···N hydrogen bonds ($d_{\text{C–H}\cdots\text{N}}$ = 2.372(3)–2.472(2) Å, Tables S1–S6 and Fig. S6†) to form a 1-D array that resembles an H-beam (Fig. 1b and 5a). In the crystalline lattice, these molecular H-beams buttress each other by C–H···π contacts. For either phenyl···triazole or phenyl···phenyl pair, the electropositive end of the C–H dipole and electronegative π-clouds of the aromatic rings establish weak C–H···π contacts ($d_{\text{C–H}\cdots\pi}$ = 3.404(3)–3.485(4) Å for phenyl···triazole; 3.517(4)–3.942(3) Å for phenyl···phenyl; Table S7†).[37] As such, the C–H dipole ends can slide freely on the π-surfaces, until the steric clash with the vertical iptycene unit stops the movement. This degree of freedom allows **1** to sample multiple packing patterns without significant energy barriers (Fig. 5b). A conceptual analogy could be drawn to a sliding door that can stop anywhere along the door track.

Depending on how these H-beam substructures are arranged in space, different polymorphs of **1** are produced (Fig. 3). The four polymorphs of **1** are structurally similar, thus making it possible for us to draw intuitive correlations and deduce the mechanism of their interconversion by molecular motions within the confines of the crystal lattice. Taking the principle of least action, the **1A**-to-**1B** transition could best be explained by horizontal sliding of the H-beam units along the central triazole–phenylene–triazole triad (Fig. 5b). On the other hand, the interconversion between **1A** and **1C** entails vertical sliding of the H-beam units along the peripheral benzene rings (Fig. 5b). More drastic rotating motions are required to interconvert porous **1B** and non-porous **1Z** (Fig. 5b). These processes are accompanied by changes in the cavity dimensions (Table S8†), which follow the order **1A** > **1B** ≫ **1C** > **1Z**.

Conclusions

Imparting dynamic properties is a powerful strategy to design stimuli-responsive porous materials.[1–11] The non-planar architecture of **1** effectively prevents close vdW contacts, thereby creating open channels. The *pseudo*-orthogonal arrangement of the π-faces constituting the H-shaped molecular scaffold functions as steric barriers for the sliding and rotating motions in the solid state. Such physical boundary conditions limit the number of possible intermolecular arrangements, thereby simplifying the reaction coordinates of their interconversion in response to external stimuli. Efforts are currently underway in our laboratory to expand this design concept, and find practical applications in host–guest chemistry.

Author contributions

T. Kang and H. Kim: conceptualization, formal analysis, investigation, methodology, visualization, writing-original draft, writing-review & editing. S. Jeoung: conceptualization, formal analysis, investigation, methodology, visualization. D. Moon: conceptualization, formal analysis, funding acquisition, methodology, supervision, validation. H. R. Moon: conceptualization, funding acquisition, supervision, validation. D. Lee: conceptualization, funding acquisition, project administration, supervision, validation, visualization, writing-original draft, writing-review & editing.

Conflicts of interest

There are no conflicts to declare.

Acknowledgements

We thank Prof. Whanchul Shin for helpful discussions. This work was supported by the Samsung Science and Technology Foundation (SSTF-BA1701-10680). The work at UNIST was supported by the National Research Foundation (NRF) of Korea (2020R1A2C3008908) funded by the Ministry of Science and ICT (MSIT). The X-ray crystallography experiments at PLS-II BL2D-SMC beamline were supported in part by MSIT and POSTECH. T. K. thanks the NRF-2016-Global PhD Fellowship Program (2016H1A2A1906550) through the NRF.

Notes and references

1 S. Das, P. Heasman, T. Ben and S. Qiu, *Chem. Rev.*, 2017, **117**, 1515–1563.

2 R.-B. Lin, Y. He, P. Li, H. Wang, W. Zhou and B. Chen, *Chem. Soc. Rev.*, 2019, **48**, 1362–1389.

3 J. R. Holst, A. Trewin and A. I. Cooper, *Nat. Chem.*, 2010, **2**, 915–920.

4 T. Tozawa, J. T. A. Jones, S. I. Swamy, S. Jiang, D. J. Adams, S. Shakespeare, R. Clowes, D. Bradshaw, T. Hasell, S. Y. Chong, C. Tang, S. Thompson, J. Parker, A. Trewin, J. Bacsa, A. M. Z. Slawin, A. Steiner and A. I. Cooper, *Nat. Mater.*, 2009, **8**, 973–978.

5 J. H. Chong, S. J. Ardakani, K. J. Smith and M. J. MacLachlan, *Chem.–Eur. J.*, 2009, **15**, 11824–11828.

6 M. I. Hashim, H. T. M. Le, T.-H. Chen, Y.-S. Chen, O. Daugulis, C.-W. Hsu, A. J. Jacobson, W. Kaveevivitchai, X. Liang, T. Makarenko, O. Š. Miljanić, I. Popovs, H. V. Tran, X. Wang, C.-H. Wu and J. I. Wu, *J. Am. Chem. Soc.*, 2018, **140**, 6014–6026.

7 T.-H. Chen, W. Kaveevivitchai, A. J. Jacobson and O. Š. Miljanić, *Chem. Commun.*, 2015, **51**, 14096–14098.

8 H. Wang, B. Li, H. Wu, T.-L. Hu, Z. Yao, W. Zhou, S. Xiang and B. Chen, *J. Am. Chem. Soc.*, 2015, **137**, 9963–9970.

9 H. Yamagishi, H. Sato, A. Hori, Y. Sato, R. Matsuda, K. Kato and T. Aida, *Science*, 2018, **361**, 1242–1246.

10 M. Mastalerz and I. M. Oppel, *Angew. Chem., Int. Ed.*, 2012, **51**, 5252–5255.

11 M. J. Bojdys, M. E. Briggs, J. T. A. Jones, D. J. Adams, S. Y. Chong, M. Schmidtmann and A. I. Cooper, *J. Am. Chem. Soc.*, 2011, **133**, 16566–16571.

12 E. A. Meyer, R. K. Castellano and F. Diederich, *Angew. Chem., Int. Ed.*, 2003, **42**, 1210–1250.

13 S. E. Wheeler, *Acc. Chem. Res.*, 2013, **46**, 1029–1038.

14 H. Choi, S. Ogi, N. Ando and S. Yamaguchi, *J. Am. Chem. Soc.*, 2021, **143**, 2953–2961.

15 S. Ueda, M. Su and S. L. Buchwald, *Angew. Chem., Int. Ed.*, 2011, **50**, 8944–8947.

16 T. Kang, H. Kim and D. Lee, *Org. Lett.*, 2017, **19**, 6380–6383.

17 V. E. Williams and T. M. Swager, *Macromolecules*, 2000, **33**, 4069–4073.

18 Y. Ramondenc, R. Schwenninger, T. Phan, K. Gruber, C. Kratky and B. Kräutler, *Angew. Chem., Int. Ed. Engl.*, 1994, **33**, 889–891.

19 R. R. Gupta, M. Kumar and V. Gupta, *Heterocyclic Chemistry Volume II: Five-Membered Heterocycles*, Springer-Verlag, Berlin Heidelberg, 1998.

20 C.-F. Chen and Y.-X. Ma, *Iptycenes Chemistry: From Synthesis to Applications*, Springer, Berlin, 2013.

21 T. M. Swager, *Acc. Chem. Res.*, 2008, **41**, 1181–1189.

22 J. H. Chong and M. J. MacLachlan, *Chem. Soc. Rev.*, 2009, **38**, 3301–3315.

23 (*a*) L. Ueberricke and M. Mastalerz, *Chem. Rec.*, 2021, **21**, 558–573; (*b*) L. Ueberricke, D. Holub, J. Kranz, F. Rominger, M. Elstner and M. Mastalerz, *Chem.–Eur. J.*, 2019, **25**, 11121–11134; (*c*) B. Kohl, K. Baumgärtner, F. Rominger and M. Mastalerz, *Eur. J. Org. Chem.*, 2019, 4891–4896.

24 M. A. Spackman and D. Jayatilaka, *CrystEngComm*, 2009, **11**, 19–32.

25 M. D. Donohue and G. L. Aranovich, *Adv. Colloid Interface Sci.*, 1998, **76–77**, 137–152.

26 S. Kitagawa and R. Matsuda, *Coord. Chem. Rev.*, 2007, **251**, 2490–2509.

27 A. Schneemann, V. Bon, I. Schwedler, I. Senkovska, S. Kaskel and R. A. Fischer, *Chem. Soc. Rev.*, 2014, **43**, 6062–6096.

28 G. Férey and C. Serre, *Chem. Soc. Rev.*, 2009, **38**, 1380–1399.

29 J. H. Lee, S. Jeoung, Y. G. Chung and H. R. Moon, *Coord. Chem. Rev.*, 2019, **389**, 161–188.

30 J. A. Mason, J. Oktawiec, M. K. Taylor, M. R. Hudson, J. Rodriguez, J. E. Bachman, M. I. Gonzalez, A. Cervellino, A. Guagliardi, C. M. Brown, P. L. Llewellyn, N. Masciocchi and J. R. Long, *Nature*, 2015, **527**, 357–361.

31 M. K. Taylor, T. Runčevski, J. Oktawiec, M. I. Gonzalez, R. L. Siegelman, J. A. Mason, J. Ye, C. M. Brown and J. R. Long, *J. Am. Chem. Soc.*, 2016, **138**, 15019–15026.

32 S. Jeoung, S. Lee, J. H. Lee, S. Lee, W. Choe, D. Moon and H. R. Moon, *Chem. Commun.*, 2019, **55**, 8832–8835.

33 S.-m. Hyun, J. H. Lee, G. Y. Jung, Y. K. Kim, T. K. Kim, S. Jeoung, S. K. Kwak, D. Moon and H. R. Moon, *Inorg. Chem.*, 2016, **55**, 1920–1925.

34 A. Comotti, S. Bracco and P. Sozzani, *Acc. Chem. Res.*, 2016, **49**, 1701–1710.

35 Q. Huang, W. Li, Z. Mao, L. Qu, Y. Li, H. Zhang, T. Yu, Z. Yang, J. Zhao, Y. Zhang, M. P. Aldred and Z. Chi, *Nat. Commun.*, 2019, **10**, 3074.

36 S. Nandi, P. De Luna, R. Maity, D. Chakraborty, T. Daff, T. Burns, T. K. Woo and R. Vaidhyanathan, *Mater. Horiz.*, 2019, **6**, 1883–1891.

37 The $d_{\text{C–H}\cdots\pi}$ values were determined by measuring the distance between the aromatic ring root-mean-square plane and the closest carbon atom of the adjacent aromatic ring in the X-ray structure. Please see Table S7† for details.